Atomistic investigation of surface characteristics and electronic features at high-purity FeSi(110) presenting interfacial metallicity

Biao Yang[a,1], Martin Uphoff[a,1], Yi-Qi Zhang[a,b,1,2], Joachim Reichert[a], Ari Paavo Seitsonen[c,d], Andreas Bauer[a], Christian Pfleiderer[a,e,f], and Johannes V. Barth[a,2]

[a]Physics Department, Technical University of Munich, Garching D-85748, Germany; [b]Institute of Physics, Chinese Academy of Sciences, 100190 Beijing, China; [c]Département de Chimie, École Normale Supérieure, F-75005 Paris, France; [d]Université de Recherche Paris-Sciences-et-Lettres, Sorbonne Université, Centre National de la Recherche Scientifique Unité Mixte de Recherche 8640, F-75005 Paris, France; [e]Munich Centre for Quantum Science and Technology (MCQST), Technical University of Munich, D-85748 Garching, Germany; and [f]Centre for Quantum Engineering (ZQE), Technical University of Munich, D-85748 Garching, Germany

Edited by Zachary Fisk, University of California, Irvine, CA, and approved March 16, 2021 (received for review October 15, 2020)

Iron silicide (FeSi) is a fascinating material that has attracted extensive research efforts for decades, notably revealing unusual temperature-dependent electronic and magnetic characteristics, as well as a close resemblance to the Kondo insulators whereby a coherent picture of intrinsic properties and underlying physics remains to be fully developed. For a better understanding of this narrow-gap semiconductor, we prepared and examined FeSi(110) single-crystal surfaces of high quality. Combined insights from low-temperature scanning tunneling microscopy and density functional theory calculations (DFT) indicate an unreconstructed surface termination presenting rows of Fe–Si pairs. Using high-resolution tunneling spectroscopy (STS), we identify a distinct asymmetric electronic gap in the sub-10 K regime on defect-free terraces. Moreover, the STS data reveal a residual density of states in the gap regime whereby two in-gap states are recognized. The principal origin of these features is rationalized with the help of the DFT-calculated band structure. The computational modeling of a (110)-oriented slab notably evidences the existence of interfacial intragap bands accounting for a markedly increased density of states around the Fermi level. These findings support and provide further insight into the emergence of surface metallicity in the low-temperature regime.

iron silicide | scanning tunneling microscopy | correlated electrons | in-gap state | surface conductivity

Iron silicide (FeSi; cf. Fig. 1*A*) is an archetypical B20 compound (1, 2) featuring a cubic unit cell without an inversion center and a remarkable sevenfold coordination of the constituents. The ε-FeSi B20 phase presents unusual temperature-dependent physical properties explored by a multitude of seminal experimental (3–13) and groundbreaking theoretical investigations guided by different conceptual approaches (14–21). There is a general consensus to classify FeSi as a prototypical *d*-electron–based narrow-gap semiconductor (gap width $\Delta < 100$ meV) whose intriguing material characteristics are strongly affected by electronic correlations and provide prospects for technological applications (21–23).

The behavior of FeSi bulk specimens in the low-temperature (LT) regime proved particularly interesting and remains an enigmatic subject. The resistivity saturates or even slightly decreases at low temperatures and exhibits a metallization at elevated temperatures, well below those nominally to be expected from the gap size (7, 24–27). Based on estimates of impurity concentrations in the samples, defect or impurity states in the gap accounting for residual conductivity were hypothesized, though also arguments in favor of intrinsic behavior exist (21). Further evidence pointing toward the existence of in-gap states has been associated with spin-polaronic phenomena (28) or localized excitonic states (29). Quite recently, two groups independently reported the detection of an electron-dominated high-mobility surface conduction channel for $T < \sim 20$ K via careful electrical transport measurements on high-purity samples of systematically varied geometric shape and Fe concentration, respectively (26, 27). Finding surface-related conduction channels would allow to reconcile the mixed metallic and semiconducting nature of FeSi at low temperatures in a simpler picture, that is, without violating the Ioffe-Regel criterion (30, 31).

The physical properties of FeSi feature striking similarities with so-called heavy-fermion semiconductors or Kondo insulators (KI), as assessed notably for $Ce_3Bi_4Pt_3$ (21, 22) or SmB_6 (32). Accordingly, FeSi was repeatedly considered as a special member of this class, although the key feature of canonical *f*-electron KIs is the hybridization between the *f* band and a conduction band. The latter entails the formation of a hybridization gap between bands of mixed character. A long-standing puzzle in exemplary KIs is an LT resistivity saturation, which was ascribed to surface conductivity (33–37). Inspired by the discovery of topological insulators, it was also proposed that KIs can host topologically protected surface states (32, 38–40). The topological KI (TKI) concept provides

Significance

Iron silicide (FeSi) provides multiple fascinating features whereby intriguing functional properties bearing significant application prospects were recognized. FeSi is understood notably as a correlated *d*-electron narrow-gap semiconductor and a putative Kondo insulator, hosting unconventional quasiparticles. Recently, metallic surface conduction channels were identified at cryogenic conditions and suggested to play a key role in the resistivity of high-quality single-crystalline specimens. Motivated by these findings, we prepared and closely examined a FeSi(110) surface with atomistically defined termination and topography. In the low-temperature regime, where surface metallicity emerges, the electronic band gap undergoes a subtle evolution. The pertaining key features, asymmetrization of the gap shape and formation of in-gap states, underscore the similarity of FeSi to unequivocal topological Kondo insulator materials.

Author contributions: C.P. and J.V.B. initially proposed this study; B.Y., M.U., and Y.-Q.Z. performed experiments; A.P.S. carried out the DFT calculations; A.B. and C.P. contributed single crystals/analytic tools; B.Y., M.U., Y.-Q.Z., J.R., A.P.S., and J.V.B. analyzed data; all authors discussed the data; and B.Y., M.U., Y.-Q.Z., J.R., A.P.S., and J.V.B. wrote the paper.

The authors declare no competing interest.

This article is a PNAS Direct Submission.

[1]B.Y., M.U., and Y.-Q.Z. contributed equally to this work.

[2]To whom correspondence may be addressed. Email: yiqi.zhang@iphy.ac.cn or jvb@tum.de.

This article contains supporting information online at https://www.pnas.org/lookup/suppl/doi:10.1073/pnas.2021203118/-/DCSupplemental.

Published April 20, 2021.

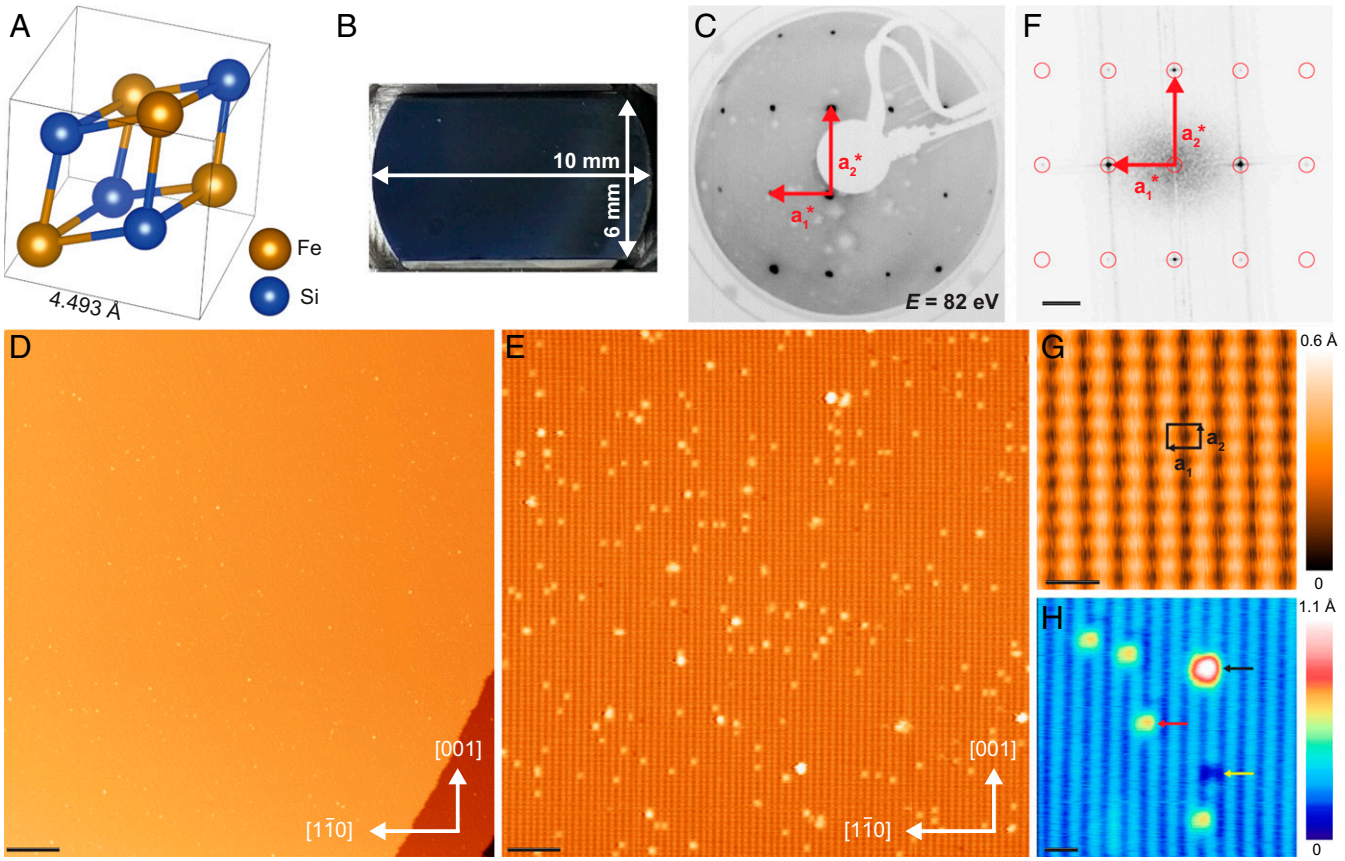

Fig. 1. Surface structure of the FeSi(110) single crystal. (*A*) FeSi B20 unit cell containing eight atoms. (*B*) Photo of the FeSi(110) single crystal (top view). (*C*) LEED pattern of FeSi(110) prepared in UHV ($E_{electron}$ = 82 eV); reciprocal lattice vectors are indicated. (*D*) Large-scale STM image of the FeSi(110) surface (V_b = −100 mV, I_t = 500 pA). (Scale bar: 20 nm.) (*E*) High-resolution STM image of a flat terrace where atomic-like features are resolved (V_b = 1 V, I_t = 100 pA). (Scale bar: 45 Å.) (*F*) 2D-FFT of *E* featuring a rectangular reciprocal lattice in good agreement with the LEED observation. (Scale bar: 0.015 $Å^{-1}$.) (*G*) Zoomed-in STM image of the surface lattice (V_b = 300 mV, I_t = 500 pA). (*H*) Representative STM image showing adatoms and vacancies on the surface (V_b = −200 mV, I_t = 1 nA). (Scale bars in *G* and *H*: 10 Å.)

a compelling explanation for robust metallic conduction channels that has been invoked in turn for FeSi (26), although earlier studies questioned the classification of FeSi as KI (12). In SmB_6, inversion of heavy quasiparticle bands at the Fermi level generates linearly dispersive heavy Dirac fermions residing in the narrow energy gap (32, 40), which were lately deduced for $T < \sim 5$ K at the $SmB_6(100)-(2 \times 1)$ reconstructed surface, inducing characteristic changes in the local density of states within the gap region (41). Related findings exist for unreconstructed $SmB_6(100)$ (42); however, there are notorious difficulties in the preparation of homogenous surfaces with this material, and certain aspects underlying the data interpretation are an unsettled matter of debate (43–45). Finally, a refined orbital-selective KI scenario was recently proposed for FeSi based on a dynamic mean-field theory analysis disentangling the eminent role of different Fe 3*d* components in the gap formation (21).

This motivated us to get an exemplary high-quality FeSi single crystal surface under control for direct scrutiny. Despite numerous investigations of FeSi samples, an atomic-level characterization of the pertaining surface characteristics and related local electronic features is missing. Cleavage methods for B20 materials provide samples of limited quality. Accordingly, angle-resolved photoemission spectroscopy (ARPES) investigations emphasized the need of well-defined surfaces and appropriate preparation protocols (8, 12), albeit the atomistic nature of the investigated systems could hitherto not be probed. First electron tunneling spectroscopic measurements were carried out on cleaved samples without recognizing the surface structure, influence of impurities, surface defects, and morphology (46).

Herein, we report on well-defined single crystalline FeSi surfaces with extended atomically flat terraces that were reproducibly prepared from polished high-quality (110)-oriented bulk samples via sputtering and annealing treatments. Employing LT-scanning tunneling microscopy (STM) as well as extensive computational modeling, we determined the surface atomic arrangement and termination with element-specific registry. Furthermore, by high-resolution scanning tunneling spectroscopy (STS) measurements, the narrow energy gap with distinct temperature-dependent characteristics is clearly resolved. For $T < \sim 10$ K, it exhibits a markedly asymmetric shape with subtle features of in-gap states located on both sides of the Fermi level, where nonzero density of states (DOS) is present. Furthermore, the band structure obtained via density functional theory (DFT) calculations of a slab with (110) surface termination reproduces key features of STS spectra in a qualitative way, showing surface-related bands crossing the bulk energy gap. Our findings confirm that samples fabricated with the highest purity standards and examined with atomistic precision are a prerequisite for both developing a basic understanding of complex materials and making further progress toward harnessing their application potential. Specifically, we provide unambiguous evidence that the appearance of surface conductivity channels for the FeSi system in the LT regime can be attributed to interfacial symmetry breaking. Moreover, our findings reveal that the electronic properties of FeSi not only resemble that of the archetypical

KI SmB_6 regarding bulk characteristics but also in the appearance of surface metallicity at low temperatures.

Results and Discussion

The 10×6 mm^2 FeSi(110) surface obtained from a high-purity bulk specimen was mirror polished (cf. Fig. 1*B*) and subsequently prepared in the ultra-high vacuum (UHV) chamber with repeated cycles of Ar^+ ion sputtering and annealing (cf. *Materials and Methods*). To monitor the surface crystallinity, in situ prepared samples were examined by low-energy electron diffraction (LEED). A distinct rectangular reciprocal pattern appears irrespective of the selected area on the whole surface and at varied electron energies (cf. Fig. 1*C* and *SI Appendix*, Fig. S1). The ratio between the reciprocal lattice vectors $\mathbf{a_1}^*$ and $\mathbf{a_2}^*$ is $1/\sqrt{2}$, consistent with the B20(110) symmetry. The pertaining lattice constants (Fig. 1*C* and *SI Appendix*, Fig. S1) are $a_{1\_LEED} = 6.3 \pm 0.1$ Å and $a_{2\_LEED} = 4.4 \pm 0.1$ Å in agreement with the reported precise value $a_0 = 4.493$ Å (cf. Fig. 1*A*) measured at liquid nitrogen temperature (3). These findings suggest that the surface is nonreconstructed.

The surface chemical composition was characterized via X-ray photoelectron spectroscopy (XPS). All characteristic peaks in the spectra can be assigned to either Fe or Si with approximately equal proportion of the constituents. A detailed scrutiny of significant energy ranges reveals that the surface is largely free from spurious carbon, oxygen, and nitrogen species (cf. *SI Appendix*, Fig. S2).

To gain further insight into the surface properties at the atomic scale, the sample topography was investigated by LT-STM. Fig. 1*D* shows a representative large-scale STM image with extended flat terraces (widths frequently exceeding 200 nm), whereby upon closer inspection, a regular one-dimensional grating structure with ≈ 6.5 Å periodicity becomes discernible (Fig. 1*E*). It is straightforward to find atomically clean patches wherein at bias voltages around 300 mV individual protrusions spanning the rectangular (110) surface lattice are clearly resolved (cf. Fig. 1*G*; the unit cell indicated comprises a single protrusion whose nature shall be clarified below). A representative two-dimensional (2D) fast Fourier transform (FFT) of the surface area (50×50 nm^2) is depicted in Fig. 1*F*, showing a rectangular lattice consistent with the LEED pattern. Via a statistical 2D-FFT analysis of atomically resolved STM images, the real-space unit cell parameters are determined to be $a_1 = 6.46 \pm 0.05$ Å and $a_2 = 4.50 \pm 0.05$ Å, in good agreement with literature values (3) and those derived from LEED.

The characteristic structural defects resolved in Fig. 1*H* are attributed to adspecies or clusters (likely related to the Fe atoms) as well as mostly single vacancies interrupting the chain-like arrangements (cf. *SI Appendix*, Fig. S3). Areas with substantial structural deficiencies or different order characteristics were only rarely observed.

In order to assess the surface atomic structure, we first determine step heights and stacking relations of adjacent terraces.

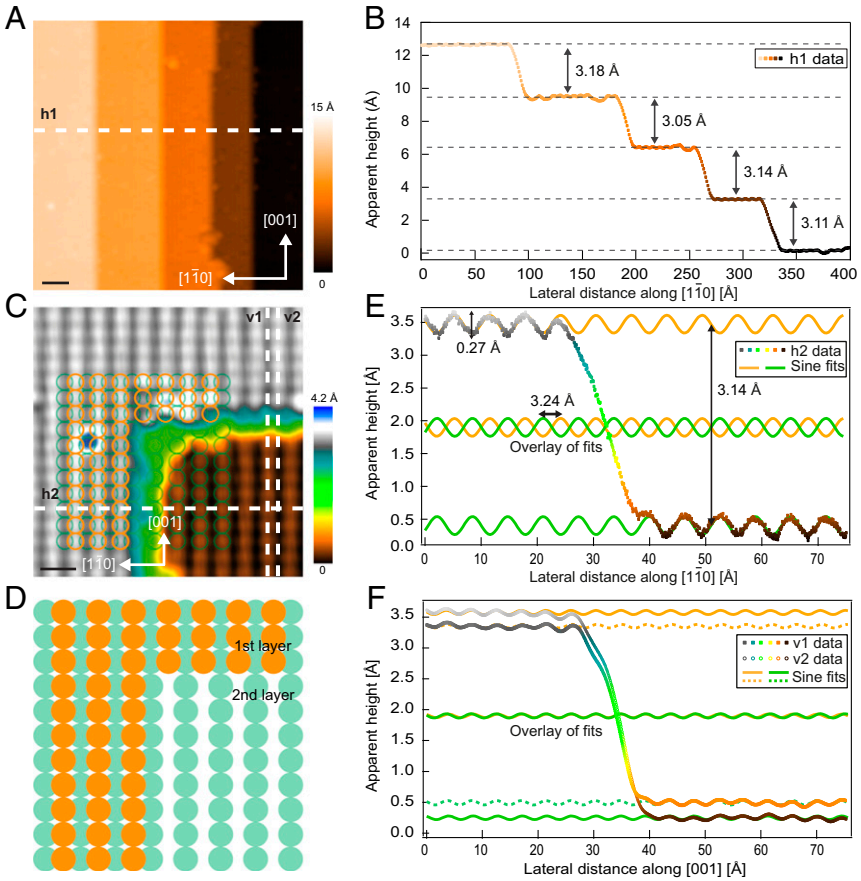

Fig. 2. FeSi(110) layer stacking. (*A*) Overview STM image of multiple steps ($V_b = -1$ V, $I_t = 55$ pA). (Scale bar: 40 Å.) (*B*) A horizontal line profile (h1 in *A*) along [1$\bar{1}$0] showing uniform step heights. (*C*) High-resolution STM image of two adjacent terraces ($V_b = 200$ mV, $I_t = 1$ nA). (Scale bar: 10 Å.) A proposed stacking model is superimposed on the STM image. Orange (green) circles coincide with the protrusion lattices in the upper (lower) terrace. (*D*) Magnified stacking model in *C*. (*E*) A horizontal line profile (h2 in *C*) fitted with sine functions on both terraces to emphasize half-unit cell shift along [1$\bar{1}$0]. The surface corrugation and step height are indicated. (*F*) Two vertical line profiles (v1 and v2 in *C*) fitted with sine functions on both terraces showing no phase shift along [001].

A statistical analysis of the step height d_{SH} (cf. Fig. 2 *A* and *B*) gives a uniform value, $d_{SH} \approx 3.1$ Å, in agreement with the bulk spacing $d_{(110)} = 3.18$ Å between adjacent isostructural (110) lattice planes. This step height is prevalent all over the sample as confirmed in many independent STM observations. The high-resolution STM image in Fig. 2*C* displays atomistic details of adjacent terraces separated by atomic steps in the high-symmetry $[1\bar{1}0]$ and [001] directions, respectively. Line profiles are taken and fitted with sine functions (Fig. 2 *E* and *F*), showing that the upper terrace lattice shifts half a unit cell with respect to the lower one along $[1\bar{1}0]$ (cf. h2 in Fig. 2*C*), that is, the rows in the first layer sit on the grooves of the second layer. The comparison of two neighboring cuts along [001] (cf. v1 and v2 in Fig. 2*C*) reveals that there is no phase shift between upper and lower rows in this direction (cf. Fig. 2*F*). For a better depiction of the stacking geometry, a scaled model of two layers is superimposed on the STM image (Fig. 2*C*) and rendered as circles in Fig. 2*D*. Overall, the FeSi(110) preparation affords homogenous isostructural surface layers with specific composition.

As a next step, extensive DFT calculations have been performed to complementarily analyze the nature of the FeSi(110) surface. Fig. 3*A* shows the multiple truncation possibilities for a B20 crystal along the (110) plane. Following the nomenclature of Krajčí et al., the planes are labeled according to their compositions of either mixed (M_i) or pure iron and silicon (F_i, S_i) (47). Note that stacking sequences along [110] are equivalent to those along $[\bar{1}10]$ due to the twofold screw rotational symmetry. Moreover, each plane features translational symmetry along [110] with $a_0/\sqrt{2}$ (3.18 Å) periodicity and a lateral shift of $a_0/\sqrt{2}$ along $[1\bar{1}0]$ (cf. Fig. 3*A*, *Right*). These features agree well with the step height and registry of adjacent terraces extracted from STM, whence the imaged (110) surface layer comprises six discrete crystal planes at different height levels.

All six possible bulk truncations (M_1, M_2, F_1, F_2, S_1, and S_2) as well as four artificial terminations with one element missing (M_1–Si, M_1–Fe, M_2–Si, M_2–Fe) have been investigated via DFT modeling. For each termination, we adopt a slab which consists of a finite number of layers (see *Materials and Methods* and *SI Appendix*). Two surfaces of each slab as well as two stacking sequences along the surface normal are identical (cf. Fig. 3*C* and *SI Appendix*, Fig. S4). Note that such constructions imply some non-stoichiometric slabs with a slight excess of one of the constituents. The surface energies were calculated considering spin-polarization effects, revealing a clear preference for interfacial spin-selective occupation of states and magnetism. Surface relaxations are small and confined to outermost layers as illustrated in Fig. 3*C* for the M_2 termination. Analogous behavior is observed for all simulated cases. The maximum vertical displacements compared to projected bulk Fe and Si locations fall below ≈ 0.1 Å (cf. Fig. 3*C*).

The surface energy can be defined as the following (48):

$$\gamma = \left(E^S - N^S_{Si}\mu_{Si} - N^S_{Fe}\mu_{Fe}\right)/A, \qquad [1]$$

where E^S is the total energy of the slab, N_i^S are the number of atoms in the slab of species i, μ_i represent the corresponding relative chemical potentials, and A is the total surface area of both sides of the slab. In nonstoichiometric cases (48), μ_{Fe} and μ_{Si} are not independent and are related by $\mu_{Fe} + \mu_{Si} = E_{coh,FeSi}$, where

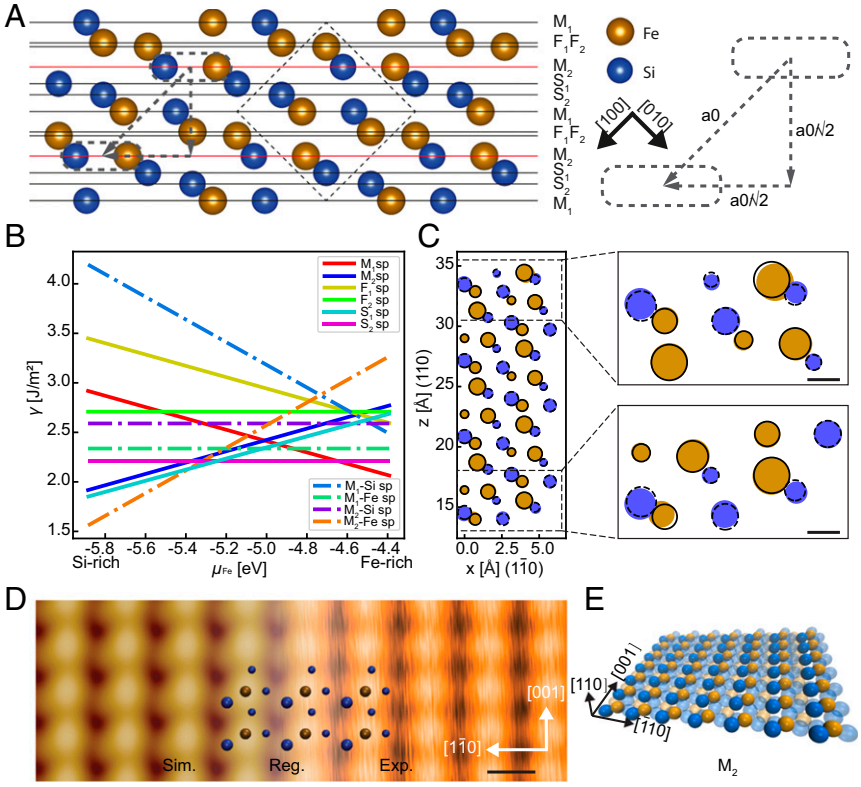

Fig. 3. Atomistic analysis and modeling of the FeSi(110) surface. (*A*) Lattice planes of FeSi(110) viewed along [001]. The dashed square indicates the projected unit cell. Paired Si–Fe atoms in adjacent M_2 layers as well as their translational symmetry are highlighted (cf. *Right* in *A*). (*B*) Surface energies of the different FeSi(110) terminations as a function of the chemical potential of Fe (μ_{Fe}) based on spin-polarized DFT calculation. (*C*) Calculated slab model with M_2 termination viewed along [001]. Hollow (solid) circles represent atomic positions before (after) relaxation. Small-surface atom displacements are magnified in *Right*. (Scale bar: 1 Å.) (*D*) Experimental STM image combined with simulated STM topography as well as scaled atomistic model of the M_2 termination. Note that smaller atoms in the model represent Si atoms below the top layer. (Scale bar: 5 Å.) (*E*) Perspective view of FeSi(110) M_2 termination. For all figures, Fe (Si) atoms are color coded in brown (blue).

$E_{coh,FeSi}$ is the cohesive energy per formula unit of FeSi. Accordingly, μ_{Fe} and μ_{Si} must be lower than their respective bulk values (47, 48), that is, $\mu_{Fe} \leq E_{coh,FeSi}$ and $\mu_{Si} \leq E_{coh,FeSi}$. We use μ_{Fe} here as the unknown parameter and its theoretical boundaries can be expressed as

$$E_{coh,FeSi} - E_{coh,Si} < \mu_{Fe} < E_{coh,Fe}. \quad [2]$$

In our case, μ_{Fe} is limited in the range of

$$-5.88\text{eV} < \mu_{Fe} < -4.39\ eV. \quad [3]$$

In Fig. 3*B*, the calculated surface energy γ for selected terminations as a function of μ_{Fe} is shown. The slope, $\frac{d\gamma}{d\mu_{Fe}} = -\frac{1}{A}(N^S_{Fe} - N^S_{Si})$, of each curve reflects the balance between the constituents in the slabs. Within the boundary conditions, M_1 reaches clearly an energy minimum on the Fe-rich side, whereas M_2, S_1, and M_2–Fe are more stable on the Si-rich side. Regarding S_2, the surface energy γ reaches a low value independent of μ_{Fe}. Thus, altogether, five terminations seem energetically feasible, that is, M_1, M_2, S_1, S_2, and M_2–Fe.

As important criterion toward identification of the preferred surface termination, constant current STM simulations for all modeled terminations using the Tersoff–Hamann approximation are compared with acquired STM data (cf. *SI Appendix*, Fig. S5). At bias voltages of ±300 mV, single protrusions are discernible in high-resolution STM (Figs. 1*G* and 3*D*, and *SI Appendix*, Fig. S5), typically without noticeable subunit cell features. Moreover, we find that there is no bias-dependent in-plane shift in the STM topography with respect to the underlying unit cell lattice (cf. *SI Appendix*, Fig. S3). Based on these criteria, terminations M_1, M_2, and S_1 can be reconciled with the STM data (cf. *SI Appendix*, Fig. S5). From a further detailed assessment and systematic survey of imaging characteristics (cf. *SI Appendix*, Figs. S6 and S7), we deduce that the best agreement holds for the M_2 termination. Fig. 3*D* displays the simulated M_2 with three outermost lattice planes superimposed on STM topography. The oval shape of the simulated protrusion (cf. *SI Appendix*, Fig. S8) therefore reflects its composition as an Fe–Si atom pair, which feature is illustrated in a perspective view (Fig. 3*E*).

To study the electronic properties of FeSi(110), we first calculated the band structure of the M_2-terminated slab, taking the influences of interfacial symmetry and electron spin polarization into account (cf. *Materials and Methods* and Fig. 4 and *SI Appendix*, Figs. S9–S11). Although the calculation is based on a simple single-particle DFT scheme, which has its limitation to describe the correlated electronic behavior (21), we observed a clear difference between the surface and bulk electronic structures. The bulk energy gap is determined to be ∼160 meV (cf. Fig. 4 *B* and *C* and *SI Appendix*, Fig. S9*B*), which is somewhat larger than previously reported experimental (21) and theoretical values (14, 16, 18). Intriguingly, in the bulk gap, additional bands derived from the slab model (red and green dotted curves in Fig. 4*B*) exist beyond the bulk electronic structure (black dotted curves in Fig. 4*B*), being both spin-polarized and crossing the Fermi level continuously. To further disentangle surface and bulk contributions, we evaluated the layer-dependent projected density of states (PDOS) characteristics (cf. *SI Appendix*, Figs. S10–S11). In Fig. 4*C*, the blue curve corresponds to the three topmost atomic layers (M_2 + S_1 + S_2, cf. Fig. 3*A*), whereas the black curve corresponds to the same layers buried in the center of the slab. Notably, the PDOS at the surface shows dissymmetric characteristics with appreciable residual intensity in the gap regime. In contrast, for the inner layers, the PDOS exhibits a rather symmetric gap boundary and is nearly vanishing around the Fermi level.

High-energy–resolution STS measurements on atomically clean areas under cryogenic conditions (liquid nitrogen temperature down to the 1.2 to 10 K range) reveal further details of the interfacial electronic characteristics. Comparative representative STS recorded on flat terraces at T_1 = 4.6 and T_2 = 78 K are depicted in Fig. 5 *A*–*D* within different bias ranges. In the overview spectra (Fig. 5*A*), a broad DOS peak, which is more prominent at 4.6 K, prevails from −500 mV to E_F. A similar feature was previously identified in ARPES measurements on FeSi(001) (49) in the same energy window and ascribed to narrow valence bands. Interestingly, we observe a continuous DOS increase for positive bias when

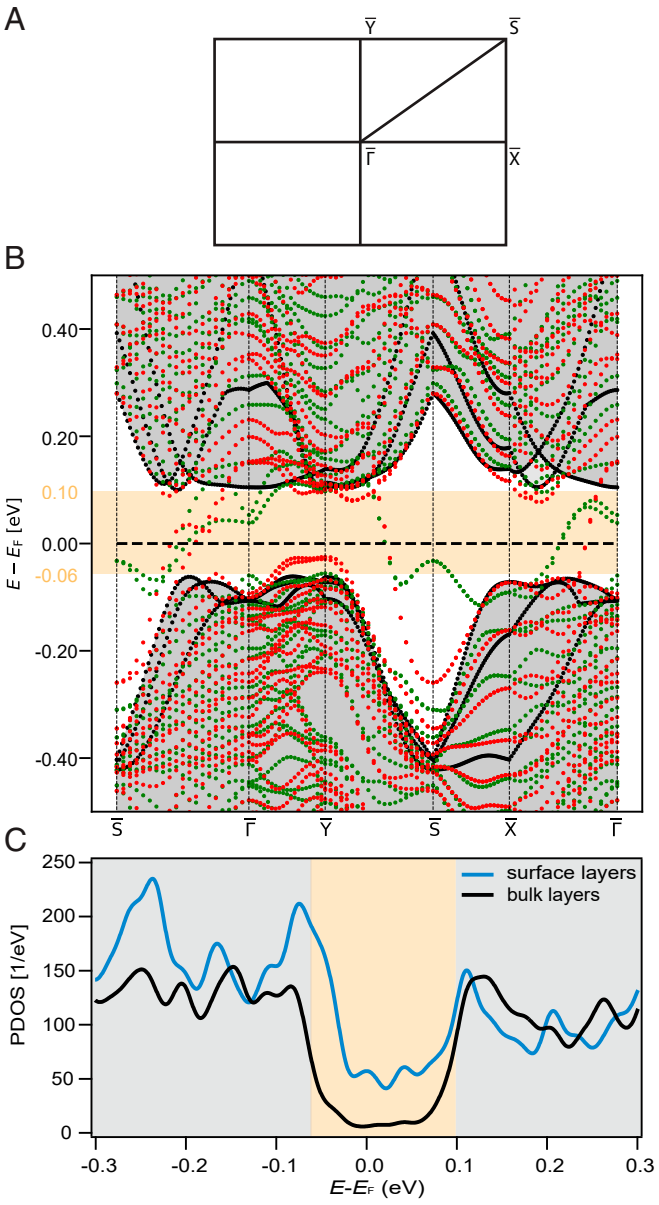

Fig. 4. DFT-calculated band structure and layer-dependent projected DOS for a M_2-terminated FeSi(110) slab. (*A*) Brillouin zone of the FeSi(110) surface. (*B*) Spin-polarized DFT calculations of the band structure of the FeSi(110) slab. The gray areas are from bulk bands projected onto the [110] direction, with the energies of the valence band maximum (−0.06 eV) and the conduction band minimum (+0.10 eV) indicated, respectively. Bands with opposite electron spins are colored in red or green, respectively. The Fermi energy is defined from the slab calculation, and the bulk-projected band structure is aligned with that from the slab calculation for best fit of valence and conduction band edges. (*C*) Projected DOS for three outermost surface layers (M_2 + S_1 + S_2) and the same layers configuration in the slab center, respectively. The gray shadow indicates the bulk band regime, and orange highlights the bulk energy gap.

sweeping up to 1 V (Fig. 5*A*), although theoretical studies of FeSi bulk band structure indicate a characteristic peak where unoccupied Fe *d*-states with strong contributions dominate the electronic structure up to ∼0.5 eV above E_F followed by a significantly reduced DOS (cf. ref. (21) and refs. therein). When focusing on a smaller bias range around E_F, a rather featureless gap signature appears at liquid nitrogen temperature that undergoes marked deepening and asymmetrization upon cooldown (Fig. 5*B*). At 4.6 K, the gap edges may be inferred from the threshold bias values where a marked change in slope occurs, and consequently, the estimated STS gap size is $E_g \approx 73$ meV (cf. *SI Appendix*, Fig. S12), coming close to the upper bound of E_g values obtained via different techniques (21). A closer inspection reveals a pronounced shoulder feature (S_1) near E_F at the occupied side of the gap edge dominated by Fe 3*d* states (Fig. 5*C*). This STS signature and the appearance of a valence band edge peak with increasing intensity and sharpening toward lower temperatures observed in photoemission experiments (10–12, 50) are expected to share a common origin. It is remarkable that this PES signature appeared for samples prepared either by cleaving and structurally well-defined FeSi(100) whence this temperature-dependent electronic structure response seems a generic material property. Moreover, similar STS characteristics were reported for SmB_6 (peak-dip feature appearing for $T < 40$ K irrespective of cleaved surface terminations) (51), an intriguing observation supporting the putative relation of the materials. A closer inspection of the STS data shown in Fig. 5 *C* and *D* reveals the emergence of additional electronic features in the gap region (labeled P_1 and P_2) that are prevalent in the sub-10 K regime as demonstrated by the temperature-dependent series of tunneling spectra in Fig. 5*E*.

For a more detailed assessment of the electronic gap and the role of the atomic surface arrangement, STS line spectra were recorded along the [1$\bar{1}$0] direction on a flat and defect-free area at $T = 1.2$ K. Fig. 6*B* shows the [−100, +100] meV window STS map from 60 line spectra in which the simultaneously recorded surface corrugation is superimposed, accounting for a weak spatial modulation (periodicity α_1). In Fig. 6*C*, the averaged STS signature and the contributions from the atomic rows versus that in the furrows are displayed, revealing merely small variations for $E > E_F$. The gap itself shows always an asymmetric V shape with its minimum located slightly above E_F (at 1.8 mV) whereby the shoulder (S_1) peaks at $E \approx -19.6$ meV (cf. *SI Appendix*, Fig. S12) Notably, a large residual DOS presents at E_F, which amounts to almost 40% of that at the gap edges (Fig. 6*C* and *SI Appendix*, Table S1). In addition, a marked bump and curvature change appear in the energy range between 0 and ≈ 50 meV (cf. *SI Appendix*, Fig. S12) associated with the in-gap electronic feature P_1 above E_F. Further details unfold in the data for the reduced [−10, +10] meV window depicted in Fig. 6 *D*–*F*. In particular, the averaged curve (60 spectra) now clearly indicates an additional in-gap electronic feature (P_2) just below the Fermi level, again with a distinct bump and curvature change. Interestingly, the P_2 contribution can be fitted with a Gaussian centered at $V_{max}(P_2) = -3.4$ mV following a gap background removal assuming a Fano-shaped signature (cf. *SI Appendix*, Fig. S12). The residual DOS at E_F together with two in-gap states (P_1, P_2) in its vicinity indicates that the in-gap electronic feature introduces metal-like behavior. Similar in-gap DOS features were observed for temperature-dependent data up to 10 K as discussed above (cf. Fig. 5 and *SI Appendix*, Table S1). The in-gap electronic structure inferred from STS can be nicely reconciled with the results of recent electronic transport studies indicating that a surface electronic conduction channel with smaller charge carrier concentration persists in the LT regime at least up to 20 K (26, 27). Moreover, it seems unlikely that the gapping characteristics and in-gap features are induced by impurities, as they are observed in atomically clean and well-defined surface regions. Specific heat measurements are also consistent with a low impurity behavior of the bulk sample used for STM/STS study (*SI Appendix*, Fig. S13). The gap characteristics were also checked in

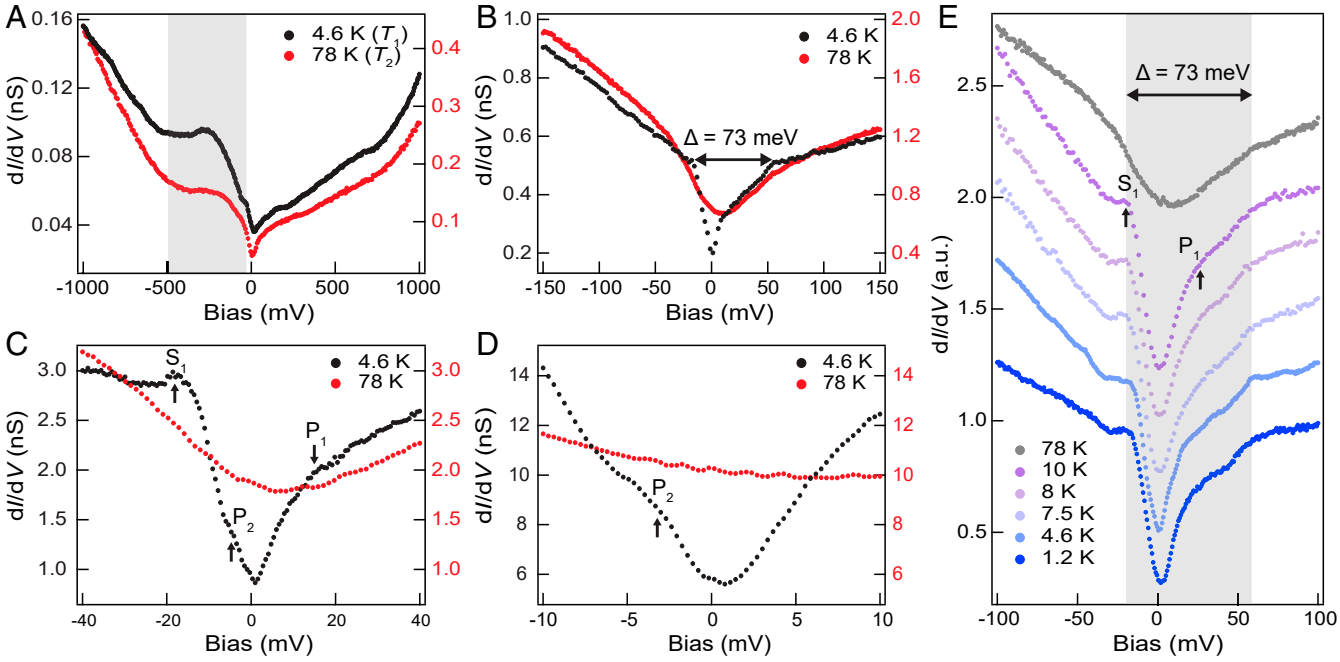

Fig. 5. STS and temperature-dependent gap characteristics of FeSi(110). (*A*–*D*) STS survey at $T_1 = 4.6$ K (LN_2) and $T_2 = 78$ K (LHe) in different bias ranges. In *A*, a prominent DOS feature between −500 mV and the Fermi level is highlighted. In *B*, the gap size is estimated to E_g ∼73 meV (cf. *SI Appendix*, Fig. S12), derived from the slope change in the d*I*/d*V* spectrum measured at 4.6 K. In *C* and *D*, three DOS features close to E_F prevalent at 4.6 K are denoted by S_1, P_1, and P_2. (*E*) Temperature-dependent evolution of dI/dV curves recorded in the gap regime. The DOS features (S_1, P_1, and P_2) and the asymmetrical gap-shape persist to $T_{meas} = 10$ K, which is the highest *T* accessible for stable STS measurements during heating.

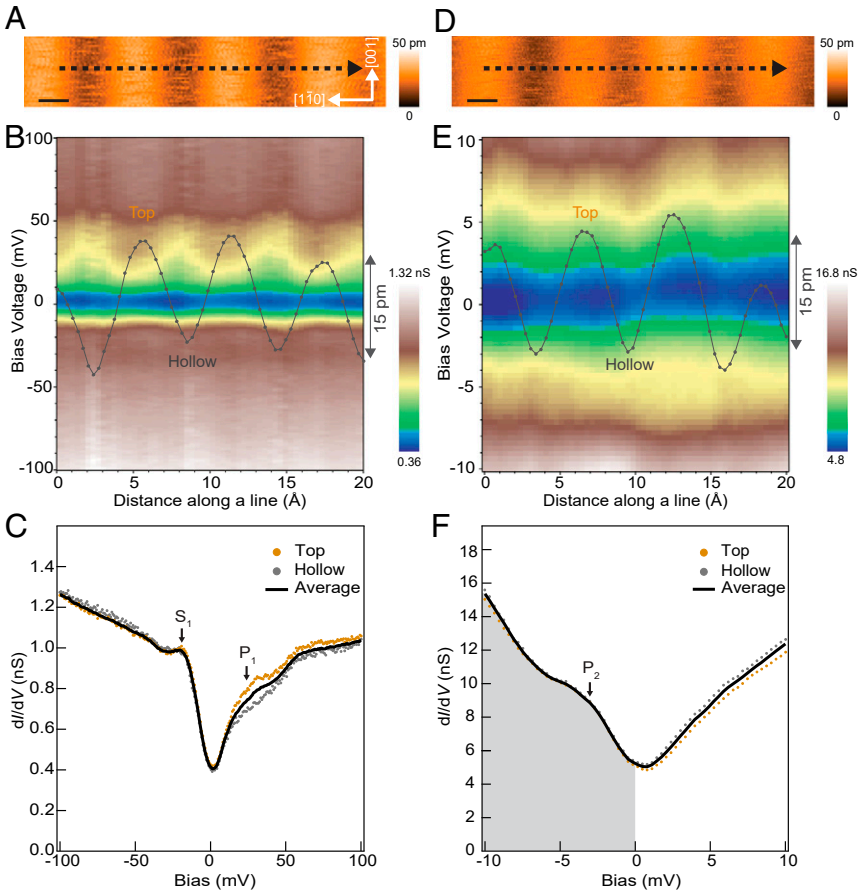

Fig. 6. Atomistic STS characterization of FeSi(110). (*A* and *D*) Reference STM images of the flat (110) terrace for STS measurements along a line [(*A*) $V_b = -100$ mV, $I_t = 100$ pA; (*D*) $V_b = -10$ mV, $I_t = 100$ pA]. Dashed lines trace STS path. (Scale bar: 2 Å.) (*B* and *E*) Color maps of total 60 dI/dV spectra taken along the line indicated in *A* and *D* with two different bias ranges. Simultaneously recorded *z* values are superimposed and reflect the surface corrugation. Top and hollow positions are labeled. (*C* and *F*) Averaged d*I*/d*V* spectra in two energy windows. The black solid curves are averaged over 60 spectra, whereas dotted brown (gray) curves are averaged over six spectra taken at the top (hollow) positions. Shaded area in *F* illustrates occupied state contributions below E_F. $T_{meas} = 1.2$ K.

the presence of atomic steps and surface vacancies (cf. *SI Appendix*, Figs. S14 and S15), small gas molecules, and organic species whereby the principal features around the Fermi level are retained.

Compared with DFT slab calculation, the primary surface-related electronic characteristics in the STS data can be understood in a qualitative way: 1) From −0.3 eV to E_F, the prominent DOS shown in Fig. 5*A* is associated with $3d_{xz}$ and $3d_{yz}$ orbitals populated with spin-polarized electrons from the topmost Fe layer (*SI Appendix*, Figs. S9 and S10*A*). Moreover, the continuous DOS increase in the unoccupied region up to 1 V may reflect a surface effect (*SI Appendix*, Figs. S9*A* and S10). 2) The shoulder feature (S_1) in the STS at the energy position of bulk valence band maximum is mainly contributed from surface Fe and Si atoms with prominent Fe $3d_{xz}$ and $3d_{yz}$ orbital character (*SI Appendix*, Fig. S11*A*). 3) The finite DOS around E_F as well as the in-gap states (cf. Fig. 6 *C* and *F*) can be associated with the surface symmetry break (Fig. 4 *B* and *C*). The calculations also reveal that at the gap boundary and in the gap region, both Fe 3*d* and Si 3*p* states are involved with a major contribution from the Fe 3*d* states (*SI Appendix*, Fig. S11 *A–D*).

In this context, it is revealing to compare the LT-induced FeSi(110) gap characteristics with tunneling spectroscopy evidence of electronic features from SmB_6 interfaces (41, 42, 51–53). Indeed, there are some remarkable, presumably systematic analogies: 1) asymmetrizing and deepening of the V-shape gap, 2) sharpening of the valance band edge peak, 3) emerging of in-gap states on both sides of E_F, and 4) a large residual DOS at E_F. Based on detailed data analysis and considering further complementary evidence, it was argued recently that the appearance of SmB_6(100) in-gap states reflects the entrance in a temperature regime where new physical properties arise, possibly because of a surface Kondo breakdown scenario setting in at $T \approx 7$ K (42) or, alternatively, the emergence of heavy Dirac surface states in line with expectations for a TKI (41).

It is worth noting that the reported FeSi bulk band structure is similar to that of other transition metal silicides with B20 structure (21, 54, 55). The special feature of FeSi is a Fermi level separating the valence and conduction bands. The band structure obtained from the DFT slab calculations provides an important hint that instead of impurity states, the surface symmetry break bestows the observed in-gap states along with a residual DOS at E_F. We infer that, in analogy to the SmB_6 system, these in-gap states could signify dispersive fermions with narrow bandwidth within the bulk gap. Notably, for FeSi(110), the in-gap state (P_1) above E_F expands in energy regions (*SI Appendix*, Fig. S12*C*), exceeding values for SmB_6 (≈ 10 meV, see refs. 41 and 42). Because of the chiral nature of B20 materials, unconventional fermions (54, 56, 57) may also play a role in the FeSi system. Moreover, the spin-polarized bands within the bulk gap point to possible surface magnetic ordering (58) (cf. *SI Appendix*, Fig. S16), elusive in bulk measurements. To detail the nature and understanding of surface metallicity

and magnetic order at FeSi interfaces, further experimental and theoretical investigations are envisioned.

Summary

In conclusion, we report atomistic insights of FeSi(110) surface and electronic properties which will underpin the development of a coherent picture of its material and interface characteristics while simultaneously highlighting the remarkable relation to *f*-metal TKIs. Unraveling the evolution of in-gap states at LT provides important implications for further classification of the nature of FeSi, including its surface conduction channels, whose origin might be closely related to the unconventional chiral fermions discovered in other B20 materials. In view of applications, engineering-correlated *d*-electron narrow band–gap semiconductors providing surface metallicity may open an alternative route to achieve dissipationless surface conduction in spintronic devices without incorporating heavy elements.

Materials and Methods

Single Crystal Growth and Sample Preparation. The FeSi(110) single crystal used in our experiments was cut from a single crystalline rod grown along the [110] direction by the optical floating zone method under UHV-compatible conditions (59). The starting elements had nominal purities of at least 99.99% for Fe and 99.9999% for Si. Combining both elements yields an impurity concentration of about 50 ppm. A small Fe deficiency of 0.005 (i.e., Fe = 0.995, Si = 1.000) was weighed in order to prevent the formation of ferromagnetic impurities. A representative $\rho(T)$ curve measured on a thin platelet FeSi(110) sample with similar growth conditions is included in the *SI Appendix*, Fig. S13. The surface dimension of the sample is ca. 10×6 mm^2 (cf. Fig. 1*B*). It was mirror polished prior to introduction in the UHV preparation chamber. The FeSi(110) crystal surface was prepared by repeated cycles of Ar^+ sputtering and annealing at ~850 to 900 K in UHV, similar to protocols in previously reported efforts (8, 12, 49).

LEED and XPS Experiments. LEED and XPS experiments were carried out in a combined UHV chamber with a base pressure below 10^{-9} mbar. LEED patterns were obtained using the SPECTALEED Optics with the sample held at ≈ 110 K. XPS measurements were carried out using the Mg Kα ($h\nu$ = 1253.6 eV) emission line of a dual-anode X-ray source. The sample position was adjusted to the normal emission geometry. The binding energy scale of FeSi(110) spectra was calibrated with the Ag3$d_{5/2}$ signal (E_b = 368.3 eV) on a Ag(111) single crystal measured in the same chamber.

STM/STS Measurements. STM/STS measurements were performed with a commercial Joule-Thomson STM (SPECS GmbH) under excellent UHV conditions (base pressure below 5.0×10^{-11} mbar). STS data were recorded predominantly at three temperatures: 1.2, 4.6, and 78 K. The STM topography images were taken in constant current mode using a W tip. The dI/dV spectra were acquired with a lock-in amplifier (frequency f = 954 Hz, and modulation V_{rms} = 0.5 to 20 mV). The tip was calibrated on a clean silver surface before and after the STS measurements, and only tips showing a clear signature of the Ag(111) surface state and otherwise a featureless DOS were employed. Since this typically implies conditioning on a chemically pure Ag(111) surface, the tip apex is presumably decorated by silver atoms. Note that we did not observe surface degradation or contamination even after weeks of measurement at 4.6 or 1.2 K, that is, under excellent vacuum conditions in the shielded cryostat.

DFT Calculations. Total energy calculations were performed using DFT within the Kohn–Sham formalism and the generalized gradient approximation (GGA) using the Quantum ESPRESSO code (60). We used the Perdew–Becke–Ernzerhof GGA and an equidistance grid of 8×12 k points in the integration over the first Brillouin zone. Projector augmented data sets were applied to remove the core electron from the explicit calculation. The bulk lattice constant was calculated initially and amounts to 4.4508 Å. Our slabs contain from 48 to 54 atoms. The lengths of the unit cell vectors in the slab calculations are 6.2944, 4.4508, and 50 Å. STM simulations were performed with the Tersoff–Hamann model using an *s*-wave tip.

Data Availability. All study data are included in the article and/or supporting information.

ACKNOWLEDGMENTS. Financial support from the Deutsche Forschungsgemeinschaft (DFG, German Research Foundation) through the Excellence Clusters Munich Center for Advanced Photonics (MAPS), and the Munich Center for Quantum Science and Technology (EXC 2111, project-id 390814868), and TRR80 (project-id 107745057) is gratefully acknowledged. This project has also received funding from the European Research Council (ERC) under the European Union's Horizon 2020 Research and Innovation Programme (grant agreement no. 788031, ExQuiSid), and Technical University of Munich (TUM) Institute of Advanced Studies, and the Munich Quantum Center. B.Y. acknowledges the TUM University Foundation and the Alexander von Humboldt-Foundation for a Research Fellowship for Postdoctoral Researchers.

1. G. Phragmén, Om järn-kisellegeringarnas byggnad. *Jernkontor. Ann.* **107**, 121 (1923).
2. L. Pauling, A. M. Soldate, The nature of the bonds in the iron silicide, FeSi, and related crystals. *Acta Crystallogr.* **1**, 212–216 (1948).
3. H. Watanabe, K. Ito, H. Yamamoto, Neutron diffraction study of intermetallic compound FeSi. *J. Phys. Soc. Jpn.* **18**, 995–999 (1963).
4. V. Jaccarino, G. K. Wertheim, J. H. Wernick, L. R. Walker, S. Arajs, Paramagnetic excited state of FeSi. *Phys. Rev.* **160**, 476–482 (1967).
5. Z. Schlesinger *et al*., Unconventional charge gap formation in FeSi. *Phys. Rev. Lett.* **71**, 1748–1751 (1993).
6. A. Damascelli, K. Schulte, D. van der Marel, A. A. Menovsky, Infrared spectroscopic study of phonons coupled to charge excitations in FeSi. *Phys. Rev. B Condens. Matter* **55**, R4863–R4866 (1997).
7. S. Paschen *et al*., Low-temperature transport, thermodynamic, and optical properties of FeSi. *Phys. Rev. B Condens. Matter* **56**, 12916–12930 (1997).
8. K. Breuer *et al*., Observation of a gap opening in FeSi with photoelectron spectroscopy. *Phys. Rev. B Condens. Matter* **56**, R7061–R7064 (1997).
9. J. F. DiTusa, K. Friemelt, E. Bucher, G. Aeppli, A. P. Ramirez, Metal-insulator transitions in the Kondo insulator FeSi and classic semiconductors are similar. *Phys. Rev. Lett.* **78**, 2831–2834 (1997).
10. K. Ishizaka *et al*., Ultraviolet laser photoemission spectroscopy of FeSi: Observation of a gap opening in density of states. *Phys. Rev. B Condens. Matter Mater. Phys.* **72**, 233202 (2005).
11. M. Arita *et al*., Angle-resolved photoemission study of the strongly correlated semiconductor FeSi. *Phys. Rev. B Condens. Matter Mater. Phys.* **77**, 205117 (2008).
12. M. Klein *et al*., Evidence for itineracy in the anticipated Kondo insulator FeSi: A quantitative determination of the band renormalization. *Phys. Rev. Lett.* **101**, 046406 (2008).
13. S. Changdar *et al*., Electronic structure studies of FeSi: A chiral topological system. *Phys. Rev. B* **101**, 235105 (2020).
14. L. F. Mattheiss, D. R. Hamann, Band structure and semiconducting properties of FeSi. *Phys. Rev. B Condens. Matter* **47**, 13114–13119 (1993).
15. D. Mandrus, J. L. Sarrao, A. Migliori, J. D. Thompson, Z. Fisk, Thermodynamics of FeSi. *Phys. Rev. B Condens. Matter* **51**, 4763–4767 (1995).
16. C. Fu, S. Doniach, Model for a strongly correlated insulator: FeSi. *Phys. Rev. B Condens. Matter* **51**, 17439–17445 (1995).
17. Y. Takahashi, Spin-fluctuation theory of FeSi. *J. Phys. Condens. Matter* **9**, 2593–2605 (1997).
18. V. V. Mazurenko *et al*., Metal-insulator transitions and magnetism in correlated band insulators: FeSi and $Fe_{1-x}Co_xSi$. *Phys. Rev. B Condens. Matter Mater. Phys.* **81**, 125131 (2010).
19. J. M. Tomczak, K. Haule, G. Kotliar, Signatures of electronic correlations in iron silicide. *Proc. Natl. Acad. Sci. U.S.A.* **109**, 3243–3246 (2012).
20. S. Khmelevskyi, G. Kresse, P. Mohn, Correlated excited states in the narrow band gap semiconductor FeSi and antiferromagnetic screening of local spin moments. *Phys. Rev. B* **98**, 125205 (2018).
21. J. M. Tomczak, Thermoelectricity in correlated narrow-gap semiconductors. *J. Phys. Condens. Matter* **30**, 183001 (2018).
22. P. S. Riseborough, Heavy fermion semiconductors. *Adv. Phys.* **49**, 257–320 (2000).
23. N. Manyala *et al*., Large anomalous Hall effect in a silicon-based magnetic semiconductor. *Nat. Mater.* **3**, 255–262 (2004).
24. M. B. Hunt *et al*., Low-temperature magnetic, thermal, and transport properties of FeSi. *Phys. Rev. B Condens. Matter* **50**, 14933–14941 (1994).
25. P. Lunkenheimer, G. Knebel, R. Viana, A. Loidl, Hopping conductivity in FeSi. *Solid State Commun.* **93**, 891–895 (1995).
26. Y. Fang *et al*., Evidence for a conducting surface ground state in high-quality single crystalline FeSi. *Proc. Natl. Acad. Sci. U.S.A.* **115**, 8558–8562 (2018).
27. M. Wagner, "Suche nach topologisch nichttrivialen Eigenschaften stark korrelierter Materialien," PhD thesis, Technical University of Munich, Munich, Germany (2014).
28. V. V. Glushkov *et al*., Spin excitations of the correlated semiconductor FeSi probed by THz radiation. *Phys. Rev. B Condens. Matter Mater. Phys.* **84**, 073108 (2011).
29. L. Degiorgi *et al*., Optical evidence of Anderson-Mott localization in FeSi. *Europhys. Lett.* **28**, 341–346 (1994).
30. N. F. Mott, Conduction in non-crystalline systems IX. The minimum metallic conductivity. *Philos. Mag.* **26**, 1015–1026 (1972).
31. A. F. Ioffe, A. R. Regel, Non-crystalline, amorphous and liquid electronic semiconductors. *Prog. Semicond.* **4**, 237 (1960).
32. M. Dzero, J. Xia, V. Galitski, P. Coleman, Topological Kondo insulators. *Annu. Rev. Condens. Matter Phys.* **7**, 249–280 (2016).
33. D. J. Kim, T. Grant, Z. Fisk, Limit cycle and anomalous capacitance in the Kondo insulator SmB_6. *Phys. Rev. Lett.* **109**, 096601 (2012).

34. X. Zhang *et al*., Hybridization, inter-ion correlation, and surface states in the Kondo insulator SmB_6. *Phys. Rev. X* **3**, 011011 (2013).
35. S. Wolgast *et al*., Low-temperature surface conduction in the Kondo insulator SmB_6. *Phys. Rev. B* **88**, 180405(R) (2013).
36. F. Chen *et al*., Magnetoresistance evidence of a surface state and a field-dependent insulating state in the Kondo insulator SmB_6. *Phys. Rev. B Condens. Matter Mater. Phys.* **91**, 205113 (2015).
37. P. Syers, D. Kim, M. S. Fuhrer, J. Paglione, Tuning bulk and surface conduction in the proposed topological Kondo insulator SmB_6. *Phys. Rev. Lett.* **114**, 096601 (2015).
38. M. Dzero, K. Sun, V. Galitski, P. Coleman, Topological Kondo insulators. *Phys. Rev. Lett.* **104**, 106408 (2010).
39. T. Takimoto, SmB_6: A promising candidate for a topological insulator. *J. Phys. Soc. Jpn.* **80**, 123710 (2011).
40. F. Lu, J. Zhao, H. Weng, Z. Fang, X. Dai, Correlated topological insulators with mixed valence. *Phys. Rev. Lett.* **110**, 096401 (2013).
41. H. Pirie *et al*., Imaging emergent heavy Dirac fermions of a topological Kondo insulator. *Nat. Phys.* **16**, 52–56 (2020).
42. L. Jiao *et al*., Additional energy scale in SmB_6 at low-temperature. *Nat. Commun.* **7**, 13762 (2016).
43. Z. H. Zhu *et al*., Polarity-driven surface metallicity in SmB_6. *Phys. Rev. Lett.* **111**, 216402 (2013).
44. E. Frantzeskakis *et al*., Kondo hybridization and the origin of metallic states at the (001) surface of SmB_6. *Phys. Rev. X* **3**, 041024 (2013).
45. P. Hlawenka *et al*., Samarium hexaboride is a trivial surface conductor. *Nat. Commun.* **9**, 517 (2018).
46. M. Fäth, J. Aarts, A. A. Menovsky, G. J. Nieuwenhuys, J. A. Mydosh, Tunneling spectroscopy on the correlation effects in FeSi. *Phys. Rev. B Condens. Matter Mater. Phys.* **58**, 15483–15490 (1998).
47. M. Krajčí, J. Hafner, Surfaces of intermetallic compounds: An *ab initio* DFT study for B20-type AlPd. *Phys. Rev. B Condens. Matter Mater. Phys.* **87**, 035436 (2013).
48. K. Reuter, M. Scheffler, Composition, structure, and stability of RuO_2(110) as a function of oxygen pressure. *Phys. Rev. B Condens. Matter Mater. Phys.* **65**, 035406 (2002).
49. M. Klein *et al*., Photoemission spectroscopy across the semiconductor-to-metal transition in FeSi. *New J. Phys.* **11**, 023026 (2009).
50. C. Park *et al*., Direct observation of a narrow band near the gap edge of FeSi. *Phys. Rev. B Condens. Matter* **52**, 16981–16984 (1995).
51. W. Ruan *et al*., Emergence of a coherent in-gap state in the SmB_6 Kondo insulator revealed by scanning tunneling spectroscopy. *Phys. Rev. Lett.* **112**, 136401 (2014).
52. S. Rößler *et al*., Hybridization gap and Fano resonance in SmB_6. *Proc. Natl. Acad. Sci. U.S.A.* **111**, 4798–4802 (2014).
53. W. K. Park *et al*., Topological surface states interacting with bulk excitations in the Kondo insulator SmB_6 revealed via planar tunneling spectroscopy. *Proc. Natl. Acad. Sci. U.S.A.* **113**, 6599–6604 (2016).
54. P. Tang, Q. Zhou, S.-C. Zhang, Multiple types of topological fermions in transition metal silicides. *Phys. Rev. Lett.* **119**, 206402 (2017).
55. D. A. Pshenay-Severin, A. T. Burkov, Electronic structure of B20 (FeSi-type) transition-metal monosilicides. *Materials (Basel)* **12**, 2710 (2019).
56. Z. Rao *et al*., Observation of unconventional chiral fermions with long Fermi arcs in CoSi. *Nature* **567**, 496–499 (2019).
57. D. S. Sanchez *et al*., Topological chiral crystals with helicoid-arc quantum states. *Nature* **567**, 500–505 (2019).
58. I. Altfeder, W. Yi, V. Narayanamurti, Spin-polarized scanning tunneling microscopy of the room-temperature antiferromagnet c-FeSi. *Phys. Rev. B* **87**, 020403(R) (2013).
59. A. Neubauer *et al*., Ultra-high vacuum compatible image furnace. *Rev. Sci. Instrum.* **82**, 013902 (2011).
60. P. Giannozzi *et al*., QUANTUM ESPRESSO: A modular and open-source software project for quantum simulations of materials. *J. Phys. Condens. Matter* **21**, 395502 (2009).